Thermal expansion and phase stability of BF$_3$ (B = Sc, Y, La, Al, Ga, In) from first principles

Hiroki Koiso[,1] Suguru Yoshida[,2] Takayuki Nagai[,3] Toshihiro Isobe,[1]
Akira Nakajima,[1] and Yasuhide Mochizuki[1,*]

[1]*Department of Materials Science and Engineering, School of Materials and Chemical Technology,*
Tokyo Institute of Technology, Tokyo 152-8550, Japan
[2]*Materials Research Institute, The Pennsylvania State University, University Park, Pennsylvania 16802, USA*
[3]*Quantum-Phase Electronics Center and Department of Applied Physics, The University of Tokyo, Bunkyo-ku, Tokyo 113-8656, Japan*

ScF$_3$ has attracted much attention because of its simple crystal structure and negative thermal expansion (NTE) over a wide temperature range. No other binary trifluoride has the same crystal structure and exhibits NTE in as wide a temperature range as ScF$_3$. There has hitherto been no sufficient explanation for this fact. Herein, to discuss the phase stability and the NTE behavior of ScF$_3$, the six binary trifluorides BF$_3$ (B = Sc, Y, La, Al, Ga, In) are thoroughly compared by using *ab initio* molecular-dynamics calculations with the on-the-fly machine-learning technique, first-principles lattice-dynamics calculations, and electronic-structure analyses based on group-representation theory and the band-unfolding method. The present study reveals that (i) the $a^-a^-a^-$ octahedral rotational distortion (ORD) in ScF$_3$ increases the frequency of the crucial phonons for realizing NTE, leading to a weakening of the NTE behavior under hydrostatic pressure; (ii) the group-representation theory predicts the emergence of ORDs triggered by the second-order Jahn-Teller effect in cubic ScF$_3$, YF$_3$, AlF$_3$, GaF$_3$, and InF$_3$; (iii) cubic ScF$_3$ and YF$_3$ do not possess ORD without pressure due to their slight orbital overlap between the cations and anions; (iv) ScF$_3$ has a delicate balance between the repulsive force term and the energy stabilization term, induced by the octahedral rotational phonon modes; and (v) metastable cubic YF$_3$ and LaF$_3$ exhibit NTE behaviors. Our findings would provide an understanding of a material-design principle for realizing NTE.

I. INTRODUCTION

Negative thermal expansion (NTE) is a counterintuitive physical property in which volume contracts with in increase in temperature. Representative NTE materials quartz, ZrW$_2$O$_8$, and ScF$_3$ were discovered in 1907 [1,2], 1968 [3], and 2010 [4], respectively, and a large amount of NTE materials have been reported, such as ReO$_3$-type [4–6], ZrW$_2$O$_8$-type [3,7–9], ZrV$_2$O$_7$-type [10,11], Sc$_2$W$_3$O$_1$2-type [12–16], NASICON-type [17–19], NbPO$_5$-type [20–22], Cu$_2$P$_2$O$_7$-type [23–25], and Cu$_2$O-type structures [26], as well as delafossites [27,28], cyanides [29–32], perovskites [33–40], and intermetallic [41] families. Although some previous studies have reported a close correlation between crystal structure and NTE [42–46], the correlation between the element, the formulation of design principles for new NTE materials, and their exploration are still challenging issues [47–53]. As an adequate case study for uncovering the correlation between the element, crystal structure, and NTE, we focus on the simple NTE material ScF$_3$ and the relevant binary trifluorides B(III)F$_3$ (B = Sc, Y, La, Al, Ga, In).

ScF$_3$ has a ReO$_3$-type structure [$Pm\bar{3}m$ phase, Fig. 1(a)] and is known to exhibit NTE in a wide temperature range (10–1100 K) [4]. On the other hand, the ground-state structures of AlF$_3$, GaF$_3$, and InF$_3$ are the distorted ReO$_3$-type structures [$R\bar{3}c$ phases, Fig. 1(b)] with the $a^-a^-a^-$ octahedral rotational distortions (ORDs) [54–56], and those of YF$_3$ and LaF$_3$ are completely different from ReO$_3$-type structure [57,58] (see Figs. S1(a) and S1(b) in Ref. [59]). The nature of NTE in ScF$_3$ is attributed to its crystal structure, which creates the low-frequency transverse phonon modes around the edge of the first Brillouin zone [61–63]. It has also been reported that local symmetry breaking in nanoparticles of ScF$_3$ weakens the NTE behavior [64,65], implying that the preservation of high space-group symmetry $Pm\bar{3}m$ is responsible for the NTE behavior of ScF$_3$. Intriguingly, ScF$_3$ is the only binary trifluoride BF$_3$ that can stably adopt the $Pm\bar{3}m$ phase even at low temperature. To the best of our knowledge, there is no detailed explanation for the reason why only ScF$_3$ can possess the high-symmetry $Pm\bar{3}m$ phase and the NTE behavior.

What determines the emergence of ORD leading to the distorted $R\bar{3}c$ phase? This question has been addressed in terms of the second-order Jahn-Teller (SOJT) theory; the emergence of ORD can be explained by covalent bond formation between Bloch states, indicating that a symmetry analysis of the electronic structure is a powerful tool [66]. However, as will be discussed later, the group theory concludes that ScF$_3$ exhibits ORD leading to low crystal symmetry, whereas the experimentally reported structure has no distortion [4], indicating the necessity of further quantitative study.

*Contact author: mochizuki.y.af@m.titech.ac.jp

In this study, to consider the correlation between the crystal structure and thermal expansion of ScF_3, we discuss the variations of mode-Grüneisen parameters and thermal expansion behaviors in the high-symmetry $Pm\bar{3}m$ and low-symmetry $R\bar{3}c$ phases for ScF_3 from first-principles lattice-dynamics and molecular-dynamics (MD) calculations. We then analyze the suppression of ORDs in ScF_3, including hypothetical cubic YF_3 and LaF_3, in detail through the group-representation theory, the band unfolding method, and crystal orbital overlap population (COOP) by comparing six $Pm\bar{3}m$ phases of BF_3 (B = Sc, Y, La, Al, Ga, In). Lastly, we predict the NTE behaviors in the metastable cubic YF_3 and LaF_3.

II. THEORETICAL BACKGROUND

A. Grüneisen parameter and negative thermal expansion

In general, the Grüneisen parameter [67] is one of the most important quantities to consider in NTE. Within the scheme of the quasiharmonic approximation (QHA), the volumetric thermal expansion coefficient α_V of a solid is expressed as [51,67–69]

$$\alpha_V = \frac{\gamma C_V}{B_T V}, \tag{1}$$

where B_T, C_V, V, and γ are the bulk modulus at a constant temperature, the heat capacity per atom at a constant volume, the volume per atom in a lattice (average atomic volume), and the Grüneisen parameter, respectively. Since B_T, C_V, and V must be positive among the variables on the right-hand side in Eq. (1), the sign of α_V depends on the sign of γ. In other words, γ should be negative when NTE is indicated. γ is expressed as a weighted average of the mode-Grüneisen parameter $\gamma_{q,\nu}$ [67] with mode-heat capacity $C_{V,q,\nu}$:

$$\gamma = \frac{\sum_{q,\nu} \gamma_{q,\nu} C_{V,q,\nu}}{\sum_{q,\nu} C_{Vq,\nu}}, \tag{2}$$

$$C_{V,q,\nu} = k_B \left(\frac{\hbar \omega_{q,\nu}}{k_B T} \right)^2 \frac{\exp(\hbar \omega_{q,\nu}/k_B T)}{[\exp(\hbar \omega_{q,\nu}/k_B T) - 1]^2}, \tag{3}$$

where $\gamma_{q,\nu}$, $C_{V,q,\nu}$, and $\omega_{q,\nu}$ are the mode-Grüneisen parameter, the mode-heat capacity at constant volume, and the frequency of the νth phonon mode in a wave vector q, respectively. As discussed above, since $C_{V,q,\nu}$ is always positive, a portion of $\gamma_{q,\nu}$ must be strongly negative for γ to be negative. $\gamma_{q,\nu}$ is defined by the volume derivative of the frequency $\omega_{q,\nu}$ of the relevant phonon mode and is expressed as

$$\gamma_{q,\nu} = -\frac{V}{\omega_{q,\nu}} \left(\frac{\partial \omega_{q,\nu}}{\partial V} \right)_T. \tag{4}$$

Here, $\gamma_{q,\nu}$ represents a portion of the anharmonicity of phonon modes, and a larger absolute value of $\gamma_{q,\nu}$ indicates stronger anharmonicity [53]. Equation (2) indicates that phonon modes with negative $\gamma_{q,\nu}$ are crucial for NTE; by calculating $\gamma_{q,\nu}$, it is possible to identify which phonon modes contribute the most to NTE. Also, by looking at the changes in these values due to the distortions, we can investigate the effect of symmetry breaking on NTE.

B. Second-order Jahn-Teller effect and irreducible representation

We describe the theoretical background of the SOJT effect below [66,70–74]. The Hamiltonian $\mathcal{H}$, which represents the energy of an electron system with an atomic displacement along a normal coordinate Q of an arbitrary phonon, is expressed as

$$\mathcal{H} = \mathcal{H}_0 + \mathcal{H}^{(1)} Q + \tfrac{1}{2} \mathcal{H}^{(2)} Q^2 + \cdots, \tag{5}$$

where $\mathcal{H}_0$ is an unperturbed Hamiltonian, and the first-order and second-order terms are given as [66,73,74]

$$\mathcal{H}^{(1)} = \left(\frac{\partial \mathcal{H}}{\partial Q} \right)_{Q=0}, \quad \mathcal{H}^{(2)} = \left(\frac{\partial^2 \mathcal{H}}{\partial Q^2} \right)_{Q=0}. \tag{6}$$

By using the perturbation theory, the total energy in the perturbed state is expressed as [66,73,74]

$$\begin{aligned} E = E_0 &+ \langle 0| \mathcal{H}^{(1)} |0\rangle Q \\ &+ \frac{1}{2} \left\{ \langle 0| \mathcal{H}^{(2)} |0\rangle - 2 \sum_n \frac{|\langle 0| \mathcal{H}^{(1)} |n\rangle|^2}{E_n - E_0} \right\} Q^2 + \cdots, \end{aligned} \tag{7}$$

where $|0\rangle$ and $|n\rangle$ represent the ground state and the nth excited state, respectively. The eigenvalues of $|0\rangle$ and $|n\rangle$ are E_0 and E_n, respectively. $\langle 0| \mathcal{H}^{(1)} |0\rangle$ is the first-order term, which takes a nonzero value only when the ground state $|0\rangle$ is orbitally degenerate [73,74], describing the first-order Jahn-Teller effect. Regarding BF_3 (B = Sc, Y, La, Al, Ga, In), there are no degenerate states because they are band insulators. Hence, we ignore the first-order term. The first term of the second-order coefficients, $\frac{1}{2} \langle 0| \mathcal{H}^{(2)} |0\rangle$, represents the short-range repulsive force induced by an atomic displacement Q. Since this term is always positive, the high-symmetry structure at $Q = 0$ is essentially preferred. On the other hand, the second term of the second-order coefficients, $-\sum_n \{|\langle 0| \mathcal{H}^{(1)} |n\rangle|^2/(E_n - E_0)\} Q^2$, indicates the degree of one-electron energy stabilization due to the atomic displacement Q. This term is always negative unless it becomes zero by a symmetry restriction. Basically, when the second term $-\sum_n \{|\langle 0| \mathcal{H}^{(1)} |n\rangle|^2/(E_n - E_0)\} Q^2$ exceeds the first term $\frac{1}{2} \langle 0| \mathcal{H}^{(2)} |0\rangle Q^2$, the structural distortion along Q is generated, implying the emergence of the imaginary phonon mode, which tends to be realized in the cases of (i) nonzero $\langle 0| \mathcal{H}^{(1)} |n\rangle$ and (ii) small energy gap $E_n - E_0$.

Here, to qualitatively analyze whether the second-order term in Eq. (7) becomes negative or not, the analysis based on group-representation theory for the term $\langle 0| \mathcal{H}^{(1)} |n\rangle$ is effective [66,73]. At first, we extract the irreducible representations (irreps) of $|0\rangle$ and $|n\rangle$ in the high-symmetry group $\mathcal{G}$, that is, Φ_0 and Φ_n from the first-principles electronic-structure calculations, while the irrep of $\mathcal{H}^{(1)}$ is identical to that of an arbitrary atomic displacement Q, which is expressed as Φ_P. And then, the direct product $\Phi_0 \otimes \Phi_P \otimes \Phi_n$ is decomposed into irreps of $\mathcal{G}$ through the wonderful orthogonality theorem [75]. If $\Phi_0 \otimes \Phi_P \otimes \Phi_n$ contains the totally symmetric representation of $\mathcal{G}$, $\langle 0| \mathcal{H}^{(1)} |n\rangle$ must be nonzero. On the other hand, if $\Phi_0 \otimes \Phi_P \otimes \Phi_n$ does not contain the totally symmetric representation, $\langle 0| \mathcal{H}^{(1)} |n\rangle$ must be zero. Because the energy

difference $E_n - E_0$ is smallest between the valence-band maximum (VBM) and the conduction-band minimum (CBM), it is reasonable to adopt the irreps of VBM and CBM as those of $|0\rangle$ and $|n\rangle$, respectively.

III. COMPUTATIONAL DETAILS

The first-principles calculations were performed using the projector-augmented-wave (PAW) method [76], the Perdew-Burke-Ernzerhof functional tuned for solids (PBEsol) within the generalized gradient approximation [77], and the Heyd-Scuseria-Ernzerhof (HSE06) hybrid functional with a Fock-exchange mixing parameter of 0.25 and a screening parameter of 0.208 Å^{-1} [78–80] as implemented in VASP [81,82]. The plane-wave cutoff energy was set to 550 eV for all the calculations, and we used PAW data sets with radial cutoffs of 0.794, 1.40, 1.59, 1.40, 1.82, 1.68, and 1.54 Å for F, Al, Sc, Ga, Y, In, and La, respectively. The following were described as valence electrons: $2s^2$ and $2p^5$ for F; $3s^2$ and $3p^1$ for Al; $4s^2$ and $3d^1$ for Sc; $4s^2$ and $4p^1$ for Ga; $4s^2$, $4p^6$, $5s^1$, and $4d^2$ for Y; $5s^2$ and $5p^1$ for In; and $5s^2$, $6s^2$, $5p^6$, and $5d^1$ for La. The PBEsol functional was used for the structural relaxation, MD calculations, and lattice-dynamics calculations, while the HSE06 hybrid functional was used for the electronic-structure calculations. All the initial crystal structures in this study were extracted from Materials Project [83]. We employed $10 \times 10 \times 10$, $8 \times 8 \times 8$, $6 \times 6 \times 9$, and $6 \times 6 \times 5$ Monkhorst-Pack k-point meshes for the ReO$_3$-type $Pm\bar{3}m$ phase, the distorted ReO$_3$-type $R\bar{3}c$ phase, the eightfold-coordinated $Pnma$ phase, and the ninefold-coordinated $P\bar{3}c1$ phase, respectively, to optimize their structures and to evaluate their total energies. The lattice constants and atomic internal coordinates were optimized until the residual stress and force converged down to 0.04 GPa and 7 meV/Å, respectively.

The *ab initio* MD calculations with the on-the-fly machine-learning technique in the isothermal-isobaric (NpT) ensemble in the range 100–700 K were carried out as implemented in VASP [84–86] with the $4 \times 4 \times 4$, $3 \times 3 \times 3$, and $2 \times 2 \times 2$ supercells for the $Pm\bar{3}m$ phase, the $R\bar{3}c$ phase, and the $Pnma$ and $P\bar{3}c1$ phases, respectively, which were extended from the relevant primitive cells. We employed a single k-point sampling for all the MD calculations. The temperature and pressure in the NpT ensemble were controlled by the Langevin method [87,88] and the Parrinello-Rahman method [89,90], respectively. The friction coefficients for the atoms and lattices were set to 1.0 and 10.0 ps^{-1}, respectively. The time increment of the velocity Verlet method was set to 2 fs, and the total number of steps was set to 20 000 (40 ps). The initial 2000 steps (4 ps) were used for a relaxation process, and the subsequent 18 000 steps (36 ps) were used for the analysis. We adopted the equilibrium volume as the average value of instantaneous volumes in all steps.

The phonon band structures were derived from the calculated force constants using PHONOPY [91–93]. We chose the supercell consisting of $2 \times 2 \times 2$ primitive cells for the $Pm\bar{3}m$ and $Pnma$ phases, that of $2 \times 2 \times 2$ conventional cells for the $R\bar{3}c$ phase, and that of $3 \times 3 \times 2$ primitive cells for the $P\bar{3}c1$ phase in order to contain all the special reciprocal points. The mode-Grüneisen parameters $\gamma_{q,\nu}$ within QHA [94] were derived from the phonon frequencies $\omega_{q,\nu}$ of the isotropically
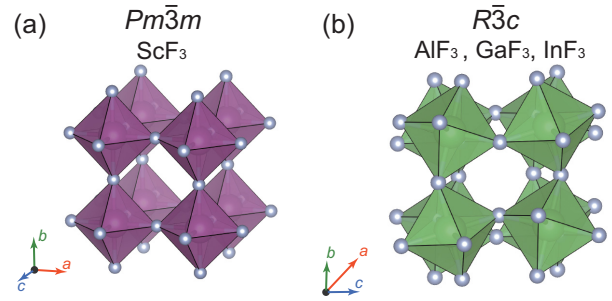

FIG. 1. Crystal structures for ScF$_3$, AlF$_3$, GaF$_3$, and InF$_3$. (a) The $Pm\bar{3}m$ phase, which is the same as the ABX_3 cubic perovskite without the A-site atom, and (b) the $R\bar{3}c$ phase that has the $a^-a^-a^-$ octahedral rotational distortions.

expanded and contracted lattice constants, which were multiplied by 1.0066 and 0.9934 with respect to the relaxed values. The atomic modulation that breaks the crystal symmetry was formed using PHONOPY [95–98]. The chemical bonding analysis through COOP was performed using LOBSTER [99–101]. The Madelung energies with the formal charges were calculated using Ewald methods as implemented in PYMATGEN [102]. The band-unfolding analyses from the $R\bar{3}c$ to $Pm\bar{3}m$ space group and the extraction of the projected electronic band structure with the density of states (DOS) were performed by using VASPKIT [103]. The symmetry analyses of phonons were performed by using AMPLIMODES [104,105] and ISODISTORT [106,107], while the symmetry analyses of electronic structures were done by using IRREP [108].

IV. RESULTS AND DISCUSSION

A. Effect of octahedral rotational distortion on thermal expansion of ScF$_3$

The previous experimental study [64,65] showed that the NTE behavior of nanoscale ScF$_3$ is weak due to the symmetry breaking associated with the $a^-a^-a^-$ ORD. To elucidate the effect of ORD in ScF$_3$ on its NTE behavior, we revisit and compare the $\gamma_{q,\nu}$ of the distorted $R\bar{3}c$ phase of ScF$_3$, which is experimentally identified under pressure higher than 0.7 GPa at 300 K [4,109]. We can see that the NTE behavior in cubic ScF$_3$ originates from the phonons at R and M points due to their largely negative $\gamma_{q,\nu}$ [Fig. 2(a)], which is identical to the previous reports [61,62]. Consistent with the experimental result, we computationally obtained the dynamically stable $R\bar{3}c$ phase of ScF$_3$ under 1.5 GPa (see Fig. S2(g) in Ref. [59]). The calculated $\gamma_{q,\nu}$ of ScF$_3$ with and without the distortions indicates that the ORDs weaken the negativity of $\gamma_{q,\nu}$ in the $Pm\bar{3}m$ phase [Fig. 2(a)]. Note that the band path of $R(1/2, 1/2, 1/2)$ to $M(1/2, 1/2, 0)$ in $Pm\bar{3}m$ is identical to the band path of $\Gamma(0, 0, 0)$ to $F(1/2, 1/2, 0)$ in $R\bar{3}c$ [Fig. 2(b)]. From the distributions of the averaged $\gamma_{q,\nu}$ of the $Pm\bar{3}m$ and $R\bar{3}c$ phases, we can confirm that the negativity of the averaged $\gamma_{q,\nu}$ is significantly weakened by the ORDs in the entire first Brillouin zone [Fig. 2(c)].

Let us see the degree of weakening of negativity for $\gamma_{q,\nu}$ at R and M in the $Pm\bar{3}m$ phase of ScF$_3$ by the ORDs in detail. Here, from the group-theoretical analysis, the irrep R_4^+ of $Pm\bar{3}m$ is found to be converted into the irreps Γ_1^+ and
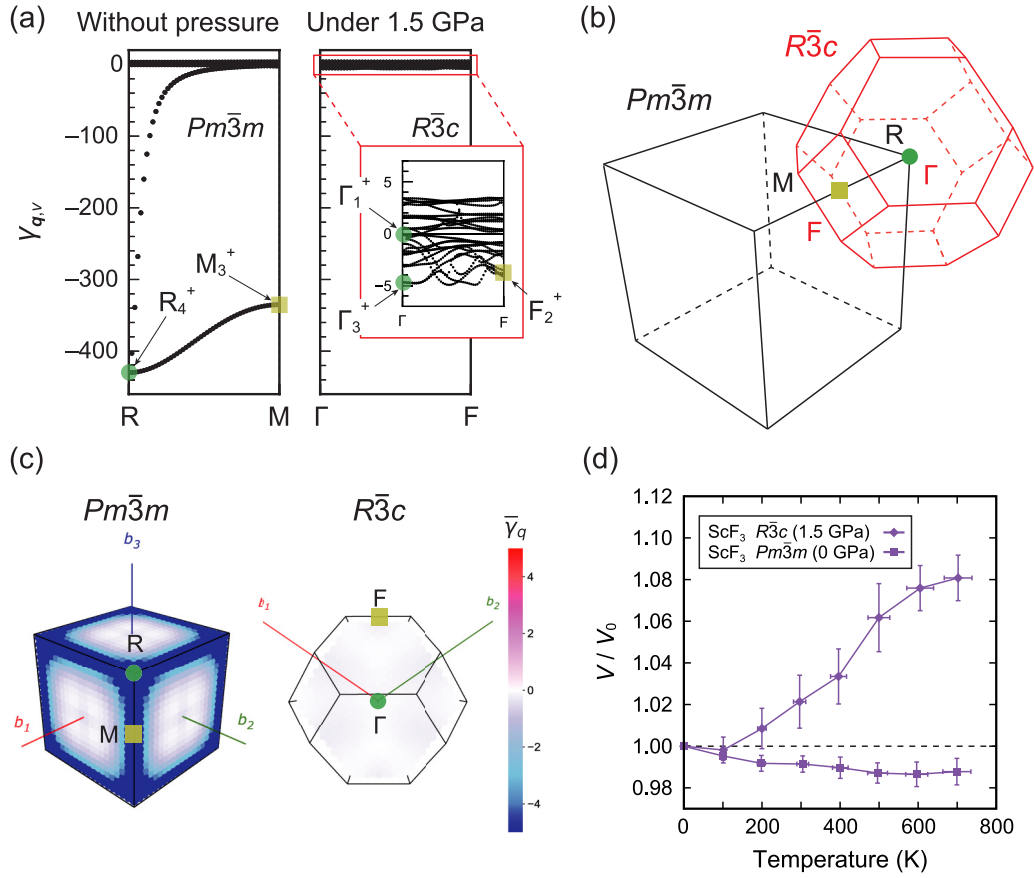
FIG. 2. (a)–(c) Comparison of mode-Grüneisen parameters $\gamma_{q,\nu}$ in the $Pm\bar{3}m$ and $R\bar{3}c$ phases of ScF$_3$. The $R\bar{3}c$ phase was obtained under hydrostatic pressure (see text for the details). (a) The dispersions of $\gamma_{q,\nu}$ of the $Pm\bar{3}m$ and $R\bar{3}c$ phases. (b) The visualized first Brillouin zone of $Pm\bar{3}m$ and $R\bar{3}c$. (c) The distributions of averaged $\gamma_{q,\nu}$ in the first Brillouin zone of $Pm\bar{3}m$ and $R\bar{3}c$ phases. The special reciprocal points Γ, R, and M of $Pm\bar{3}m$ are located at $\Gamma(0, 0, 0)$, $R(1/2, 1/2, 1/2)$, and $M(1/2, 1/2, 0)$, respectively. The R and M points of $Pm\bar{3}m$ are transformed into $\Gamma(0, 0, 0)$ and $F(1/2, 1/2, 0)$ of $R\bar{3}c$, respectively. (d) Equilibrium lattice volumes of the $Pm\bar{3}m$ phases without pressure and $R\bar{3}c$ phases under 1.5 GPa for ScF$_3$ extracted from the *ab initio* molecular-dynamics calculations performed with the on-the-fly machine-learning force field. The error bars as the standard deviations for temperature and volumes are also indicated.

Γ_3^+ of $R\bar{3}c$, while the irrep M_3^+ of $Pm\bar{3}m$ is converted into the irrep F_2^+ of $R\bar{3}c$. As enumerated in Table I, we obtained $\gamma_{q,\nu}$ of the Γ_1^+ and Γ_3^+ (F_2^+) phonons in the distorted $R\bar{3}c$ phases that existed as the R_4^+ (M_3^+) phonons in the $Pm\bar{3}m$ phase. As can be seen in Table I and Figs. 2(a) and 2(c), the negativity of $\gamma_{q,\nu}$ in the $R\bar{3}c$ phase of ScF$_3$ is significantly weakened, which is comparable to those in $B'F_3$ ($B' =$ Al, Ga, In) (see Table S1 in [59]). From Eq. (4), one can see that a low $\omega_{q,\nu}$ gives rise to a largely negative $\gamma_{q,\nu}$ when $(\partial\omega_{q,\nu}/\partial V)_T$

is positive. Thus, the weakening of the negativity for $\gamma_{q,\nu}$ is attributed to both the increase of $\omega_{q,\nu}$ and the decrease of $(\partial\omega_{q,\nu}/\partial V)_T$ for the R_4^+ and M_3^+ phonons due to the ORDs (see the values of $\omega_{q,\nu}$ and $(\partial\omega_{q,\nu}/\partial V)_T$ in Table I), which explain the experimental reports of weakened NTE behavior of ScF$_3$ nanoparticles [64,65].

To further consider the thermal-expansion behaviors of the $Pm\bar{3}m$ and $R\bar{3}c$ phases for ScF$_3$, we also calculated the equilibrium lattice volumes from the *ab initio* MD calculations with the on-the-fly machine-learning technique [Fig. 2(d)]. We have found that the PTE behaviors are observed in the $R\bar{3}c$ phase of ScF$_3$ under 1.5 GPa [Fig. 2(d)]. These results are consistent with the weakened negativity of mode-Grüneisen parameters in the $R\bar{3}c$ phase [Table I]. Note that, in Sec. I in Ref. [59], we discuss the reproducibility of thermal-expansion behaviors from the MD calculations for the ground-state structures of six BF$_3$ [Fig. S1(c)] by comparing them with the experimental values [4,54,110,111].

The effect of the weakening of the negativity for $\gamma_{q,\nu}$ due to the ORDs would be generalized to the PTE behavior of $B'F_3$ ($B' =$ Al, Ga, In) and other compounds. In AlF$_3$, the previous experimental reports [54] have shown that the $Pm\bar{3}m$ ($R\bar{3}c$) phase is realized in temperatures higher (lower) than

TABLE I. Irreducible representations, frequencies in units of THz, mode-Grüneisen parameters $\gamma_{q,\nu}$, and volume derivatives of frequencies in units of THz/Å^3 of ScF$_3$ for the $Pm\bar{3}m$ phase without pressure and the $R\bar{3}c$ phase under 1.5 GPa.

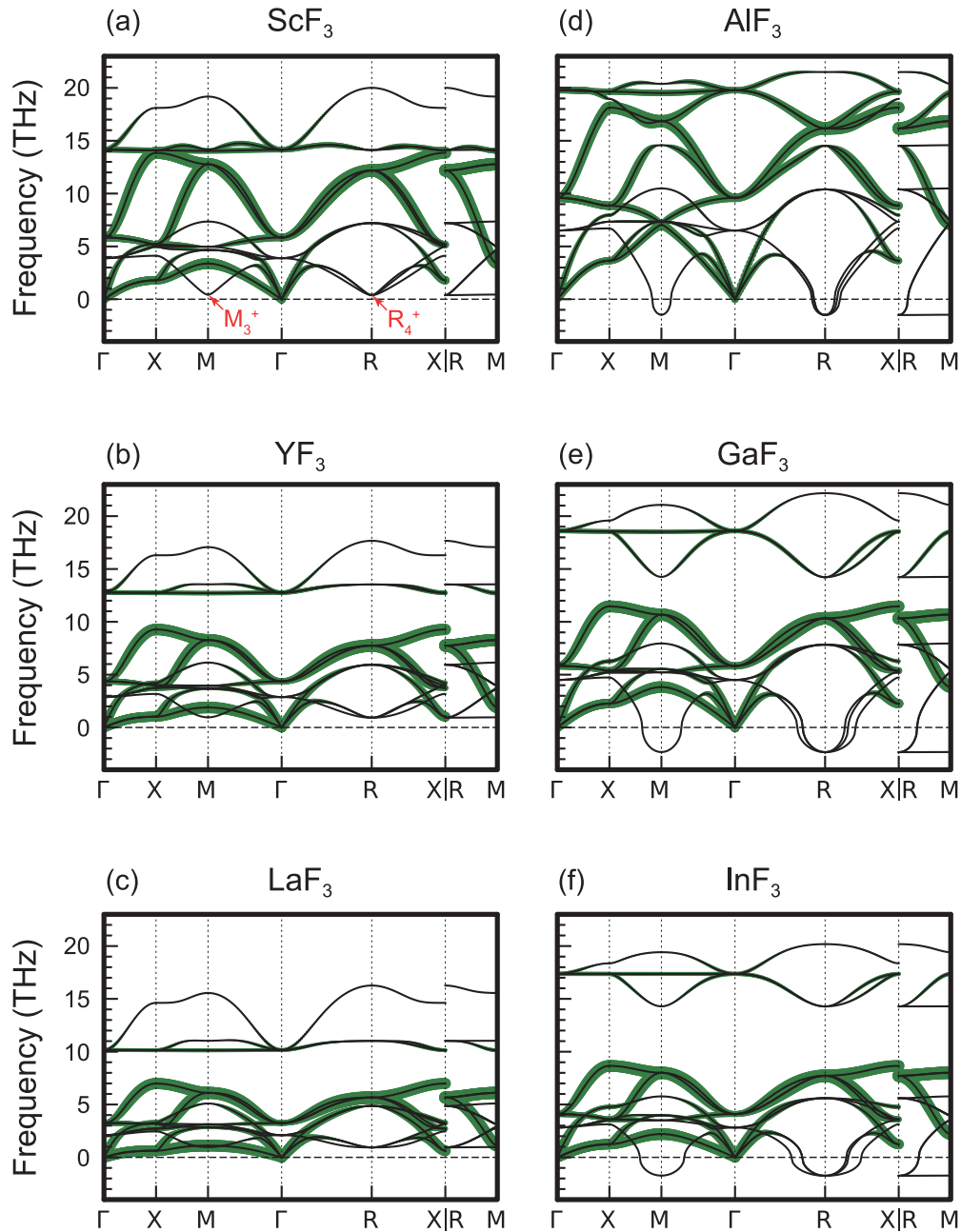| Space group	Irrep	$\gamma_{q,\nu}$	$\omega_{q,\nu}$	$(\partial\omega_{q,\nu}/\partial V)_T$
$Pm\bar{3}m$	R_4^+	-430	0.389	2.62
	M_3^+	-335	0.439	2.31
	Γ_1^+	-9.03×10^{-3}	6.07	4.93×10^{-4}
$R\bar{3}c$	Γ_3^+	-4.67	3.16	0.133
	F_2^+	-3.78	3.48	0.118

FIG. 3. Calculated phonon band structures for (a) ScF_3, (b) YF_3, (c) LaF_3, (d) AlF_3, (e) GaF_3, and (f) InF_3 of the $Pm\bar{3}m$ phases. The green circles indicate the relative degree of projected mode amplitudes of the relevant cations.

700 K, and the volumetric thermal-expansion coefficients of the $Pm\bar{3}m$ phase are lower than those of the $R\bar{3}c$ phase. Moreover, in double-ReO$_3$-type CaTiF$_6$, it has been experimentally reported that the undistorted cubic $Fm\bar{3}m$ (distorted $R\bar{3}$) phase is realized in temperatures higher (lower) than 110 K, exhibiting NTE (PTE) behavior [54]. In addition, TaO$_2$F, which resembles ReO$_3$, has been reported not to exhibit NTE behavior because of its local structural distortion [112].

B. Suppression of octahedral rotational distortions in ScF$_3$

To shed light on the dynamical properties of ORDs, phonon bands are calculated [Fig. 3] for the $Pm\bar{3}m$ phase of the six BF$_3$, which is, however, totally hypothetical for YF$_3$ and

LaF$_3$. Here, the size of the green circles in the phonon bands [Fig. 3] indicates the relative degree of projected vibration mode amplitudes of cations. We have found that BF$_3$ of the $Pm\bar{3}m$ phase becomes dynamically stable when the B-site cation is composed of early-transition metal [Figs. 3(a)–3(c)], whereas it becomes dynamically unstable if the B-site cation is composed of post-transition metal [Figs. 3(d)–3(f)]. The imaginary phonon modes at R and M in B'F$_3$ ($B' = $ Al, Ga, In) transform as irreps R_4^+ and M_3^+, respectively, which are responsible for the NTE behavior in ScF$_3$. Figure 3 shows that the phonon modes transforming as R_4^+ and M_3^+ do not contain the vibration of cations, reconfirming that those phonon modes are composed of the vibration of fluorine.
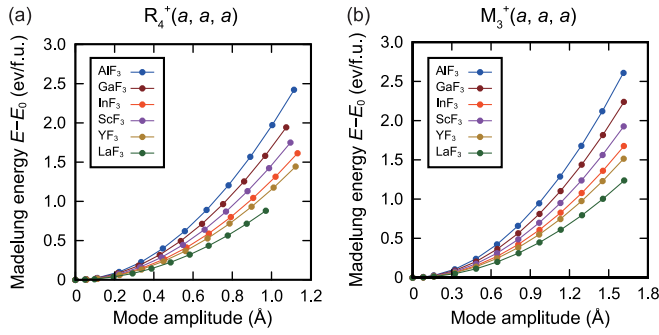
FIG. 4. Relative Madelung energies of six metal trifluorides as a function of the mode amplitudes transforming as irreducible representations (a) $R_4^+(a, a, a)$ and (b) $M_3^+(a, a, a)$.

To consider the origin of ORDs, we calculated relative Madelung energies of the distorted $R\bar{3}c$ and $Im\bar{3}$ phases, which are isotropy subgroups of $Pm\bar{3}m$ corresponding to irreps $R_4^+(a, a, a)$ and $M_3^+(a, a, a)$, respectively [Fig. 4], by using the formal charges. The previous computational study of antiperovskites [113] has shown that the ORDs transforming like irreps R_4^+ and M_3^+ reduce the Madelung energies, leading to a lowering in the total energies. However, in the case of BF$_3$, the ORDs increase their Madelung energies. These results clarify that the nonclassical effect is essential to consider the dynamical stability of BF$_3$, which cannot be considered in the Madelung energy. The nonclassical effect should be investigated to determine whether the VBM and CBM are hybridized or not under the ORD.

To uncover whether the hybridization of VBM and CBM is symmetrically permitted or not under the ORD, we analyze the irreps of VBM and CBM with the atomic displacement transforming as irrep R_4^+ in the $Pm\bar{3}m$ phase in the same way as in the previous studies [66,74]. The calculated band gaps, the irreps of VBM and CBM, the bond lengths of B and F, and the relative total energy of cubic BF$_3$ are enumerated in Table II (see Fig. S3 for the calculated electronic band structures with the full band paths for the six $Pm\bar{3}m$ phases in Ref. [59]). By using these irreps, we calculate the direct product $\Phi_0 \otimes \Phi_P \otimes \Phi_n$ and obtain the decomposed irreps of the $Pm\bar{3}m$ phases for ScF$_3$ as

$$R_4^+ \otimes R_4^+ \otimes \Gamma_5^+ = \Gamma_1^+ + \Gamma_2^+ + 2\Gamma_3^+ + 3\Gamma_4^+ + 4\Gamma_5^+, \quad (8)$$

TABLE II. Irreducible representations of VBM and CBM, band gaps ε_g calculated within the HSE06 functional, bond lengths l_{B-F} between B and F, and energies above hull ΔE (relative total energies with respect to the ground-state phases) for six BF$_3$ of the $Pm\bar{3}m$ phases calculated within the PBEsol functional.

Compound	VBM	CBM	ε_g (eV)	l_{B-F} (Å)	ΔE (eV/atom)
ScF$_3$	R_4^+	Γ_5^+	8.39	2.00	0
YF$_3$	R_4^+	Γ_1^+	9.28	2.16	6.30×10^{-2}
LaF$_3$	Γ_4^-	Γ_1^+	8.65	2.31	1.43×10^{-2}
AlF$_3$	R_4^+	Γ_1^+	9.98	1.80	3.18×10^{-3}
GaF$_3$	R_4^+	Γ_1^+	6.55	1.90	2.69×10^{-2}
InF$_3$	R_4^+	Γ_1^+	5.81	2.09	2.02×10^{-2}

while in the cases of B'F$_3$ ($B' =$ Al, Ga, In) and YF$_3$, the direct product is expressed as

$$R_4^+ \otimes R_4^+ \otimes \Gamma_1^+ = \Gamma_1^+ + \Gamma_2^+ + \Gamma_3^+ + \Gamma_4^+ + \Gamma_5^+. \quad (9)$$

These results indicate that the ORD transforming as irrep R_4^+ would be generated in these five compounds because the totally symmetric representation Γ_1^+ is included in Eqs. (8) and (9). On the other hand, the direct product of the $Pm\bar{3}m$ phase for LaF$_3$ is expressed as

$$\Gamma_4^- \otimes R_4^+ \otimes \Gamma_1^+ = R_1^- + R_3^- + R_4^- + R_5^-. \quad (10)$$

As for the $Pm\bar{3}m$ phase of LaF$_3$, the emergence of ORD is not expected because Eq. (10) does not contain Γ_1^+. These analyses based on group-representation theory for B'F$_3$ ($B' =$ Al, Ga, In) and LaF$_3$ are consistent with their phonon bands, while those for ScF$_3$ and YF$_3$ are not fully addressed to their phonon bands, indicating the necessity of a quantitative discussion (see Sec. IV for further analyses on the electronic states other than VBM and CBM by using the group-representation theory in Ref. [59]).

To investigate the degree of the hybridization of VBM and CBM due to the ORDs in BF$_3$, we directly compare the electronic structures between the $Pm\bar{3}m$ and $R\bar{3}c$ phases, as illustrated in Fig. 5. Here, the size of the red circles in Fig. 5 indicates the degree of the relevant projected DOS of cations s or d states. Note that we applied the band-unfolding method [114,115] to the electronic structures of the distorted $R\bar{3}c$ phases. Moreover, we unified the degree of ORDs in BF$_3$ for comparison in Fig. 5; the bond angle of B–F–B is unified to 172.6°. This degree of distortion amplitude yields a small total-energy change as $+2$ meV/f.u. with respect to the $Pm\bar{3}m$ phase in ScF$_3$ so that the distorted structures can be treated as perturbed systems. We denote here that energies below 1 meV/f.u. are treated as numerical errors.

From Fig. 5, we can observe the variations in the electronic structures around VBM. In AlF$_3$, GaF$_3$, and InF$_3$, we can see the comparatively large band splits of threefold-degenerate states at VBM, whereas the slight band splits are shown in ScF$_3$, YF$_3$, and LaF$_3$. Note that the threefold-degenerate R_4^+ electronic state splits into nondegenerate Γ_1^+ and twofold-degenerate Γ_3^+, while the threefold-degenerate Γ_4^- state in cubic LaF$_3$ splits into nondegenerate Γ_2^- and twofold-degenerate Γ_3^- in the $R\bar{3}c$ phase by the ORD. Additionally, due to the ORDs, the cation B'-s states ($B' =$ Al, Ga, In) are hybridized into the valence bands in B'F$_3$, whereas the d states (s states) of ScF$_3$ (YF$_3$ and LaF$_3$) are less hybridized. These electronic-structure analyses indicate the emergence of ORD in AlF$_3$, GaF$_3$, and InF$_3$ [Figs. 3(d)–3(f)], and the suppression of ORD in the $Pm\bar{3}m$ phases of ScF$_3$, YF$_3$, and LaF$_3$ [Figs. 3(a)–3(c)].

Herein, we consider the suppression of ORD in ScF$_3$ in terms of bond length, band gap, and orbital overlap by comparing ScF$_3$, AlF$_3$, and InF$_3$ because of the qualitative prediction of the group representation theory. As discussed in Sec. II, the energy-stabilization term $-\sum_n \{| \langle 0| \mathcal{H}^{(1)} |n\rangle |^2/(E_n - E_0)\} Q^2$ should have a largely negative value under the conditions of (i) large $| \langle 0| \mathcal{H}^{(1)} |n\rangle |^2$ and/or (ii) small $E_n - E_0$. When we compare AlF$_3$ and ScF$_3$, the bond length of AlF$_3$ is shorter than ScF$_3$, while the band gap of AlF$_3$ is larger than that of ScF$_3$. The shorter
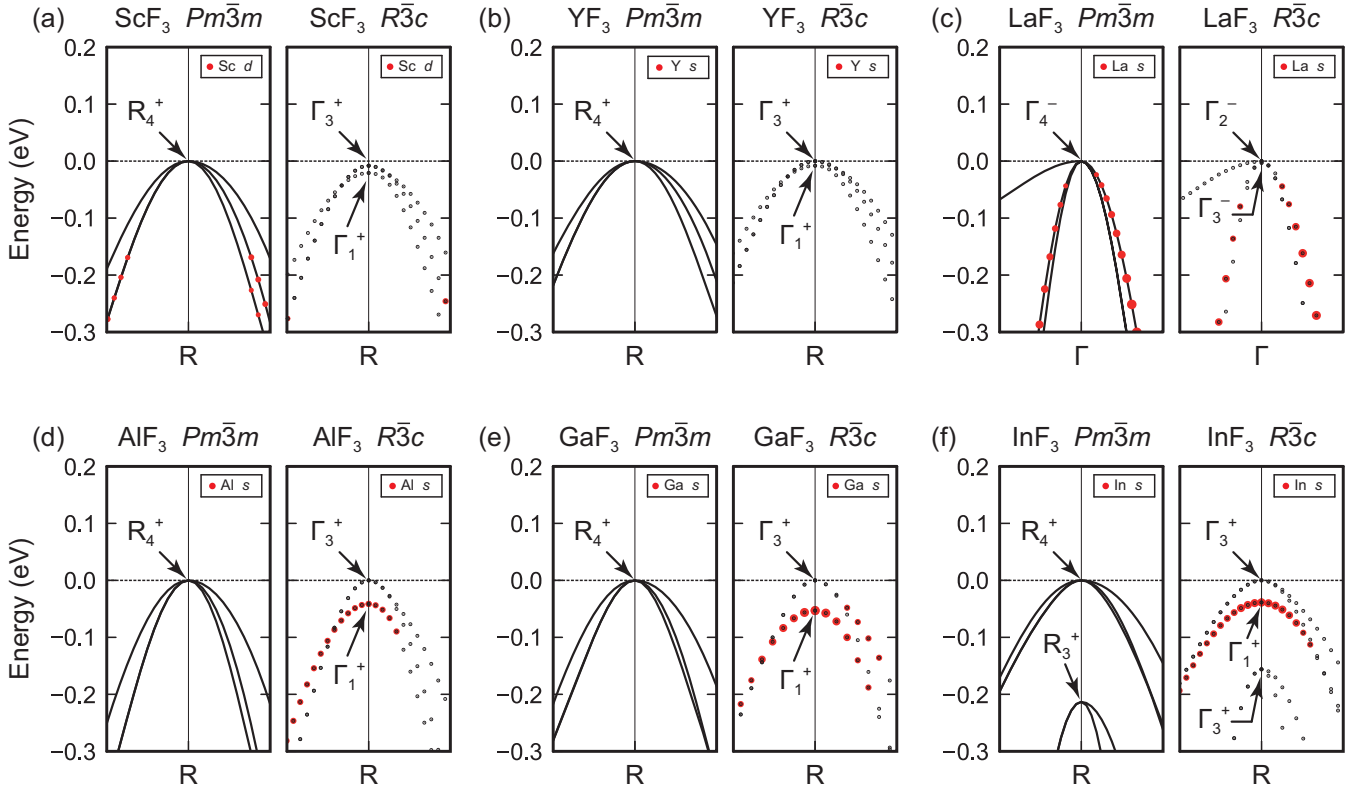
FIG. 5. Calculated electronic band structures with and without the octahedral rotational distortions for (a) ScF_3, (b) YF_3, (c) LaF_3, (d) AlF_3, (e) GaF_3, and (f) InF_3 by using the HSE06 hybrid functional in the vicinity of VBM. All of the band structures of the $R\bar{3}c$ phases are unfolded into the first Brillouin zone of $Pm\bar{3}m$. The black dots in the $R\bar{3}c$ phase band structures represent the band edge with the spectral weight over 50%. The B–F–B bond angles of the $Pm\bar{3}m$ and $R\bar{3}c$ phases are, respectively, 180° and 172.6°. The relevant $R\bar{3}c$ structures (B–F–B = 172.6°) were generated by equidistantly separating the relaxed $Pm\bar{3}m$ and the $R\bar{3}c$ phases. The red circles represent the degree of the relevant projected DOS.

bond length of AlF_3 gives rise to a comparatively larger crystal orbital overlap, which should lead to a large value of $|\langle 0|\mathcal{H}^{(1)}|n\rangle|^2$. As enumerated in Table III, we calculated the integrated COOPs (iCOOPs) of the distorted $R\bar{3}c$ phases of the six BF_3. Here, for the calculation of iCOOPs, we unified the bond angle of B–F–B in the same way as in Fig. 5. One can see that the iCOOP of AlF_3 is three times larger than that of ScF_3, implying the larger value of $|\langle 0|\mathcal{H}^{(1)}|n\rangle|^2$ in AlF_3. On the other hand, as for the comparison between InF_3 and ScF_3, the bond length of InF_3 is comparable with that of ScF_3, while the band gap of InF_3 is smaller than ScF_3

[Table III]. Although the bond lengths of InF_3 and ScF_3 are comparative, the iCOOP of InF_3 is about 2.5 times larger than that of ScF_3 because the orbital size of $5s$ states is far larger than that of $3d$ states.

In short, in ScF_3, the repulsive force term $\frac{1}{2}\langle 0|\mathcal{H}^{(2)}|0\rangle Q^2$ is slightly larger than the energy stabilization term $-\sum_n\{|\langle 0|\mathcal{H}^{(1)}|n\rangle|^2/(E_n - E_0)\}Q^2$ without pressure. From the relative total energy of the distorted $R\bar{3}c$ phase as a function of the R_4^+ atomic displacement in ScF_3, we can confirm that the coefficient of the quadratic term is almost zero (see Fig. S4 and Sec. V in Ref. [59]), leading to the very low frequency of the R_4^+ phonon [Fig. 3(a)] and the strongly anharmonic relative total energy due to the R_4^+ phonon. As discussed in Eq. (8), the emergence of ORD was qualitatively predicted by the group-representation theory for ScF_3, which, in fact, does not contradict the experimental result: we consider that the energy-stabilization term, namely the SOJT effect in ScF_3, is extremely scarce without pressure because of its large band gap and its long bond length. Indeed, we have confirmed the tiny hybridization of Sc-$3d$ and F-$2p$ states, which triggers the little band split [Fig. 5(a)] and slight band-gap opening [Table III] induced by the ORD in ScF_3. We also consider that the delicate balance between the two terms in ScF_3 should explain the experimentally reported quantum phase transition of ScF_3 [116].
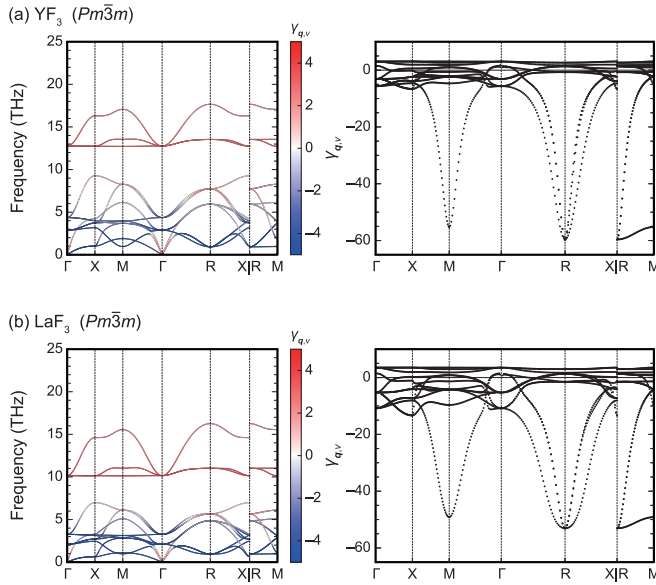
TABLE III. Integrated COOPs (iCOOPs) up to VBM between the B–F bonds for the $R\bar{3}c$ phases of six BF_3, the band-gap changes $\Delta\varepsilon_g$ due to the ORD with the bond angle of B–F–B as 172.6°.

Compound	iCOOPs (eV)	$\Delta\varepsilon_g$ (eV)
ScF_3	0.040	0.023
YF_3	0.062	0.019
LaF_3	0.038	0.008
AlF_3	0.120	0.134
GaF_3	0.121	0.316
InF_3	0.104	0.277

FIG. 6. Calculated phonon band structures and mode-Grüneisen parameters $\gamma_{q,\nu}$ for the metastable $Pm\bar{3}m$ phases of (a) YF$_3$ and (b) LaF$_3$ without hydrostatic pressure.

C. Negative thermal expansion in metastable cubic YF$_3$ and LaF$_3$

We have shown that the COOPs between the early-transition metals (Sc, Y, La) and fluorine are scarce, leading to the suppression of ORD, whereas those between the post-transition metals (Al, Ga, In) and fluorine are large [Table III] leading to the emergence of ORD. This perspective gives us an expectation that the metastable $Pm\bar{3}m$ phases of YF$_3$ and LaF$_3$ would possess NTE behavior. Intriguingly, the metastable $Pm\bar{3}m$ phases of YF$_3$ and LaF$_3$ have negative Grüneisen parameters at R and M points [Fig. 6], which are analogous to ScF$_3$. Notably, the relative total energy of cubic YF$_3$ with respect to the ground-state phase is comparable to that of cubic GaF$_3$ [Table II]. We also present the *ab initio* MD calculation results for the cubic YF$_3$ and LaF$_3$ [Fig. 7], indicating their NTE behaviors. The prominent NTE behaviors can be observed as the cation size increases. This phenomenon can be understood from the perspective of average atomic volume, which is defined as the lattice volume divided by the number of atoms in the lattice: the larger average atomic volume yields the stronger NTE behaviors [27] because the most crucial R_4^+ and M_3^+ low-energy transverse phonons make the anions vibrate forward to vast void space (void A-site in ABX_3 cubic perovskite structure) [53]. Note that the calculated equilibrium average atomic volumes at 300 K for the cubic ScF$_3$, YF$_3$, and LaF$_3$ are 15.82, 20.04, and 24.36 Å^3, respectively. Here, we also denote that the Grüneisen parameters at R and M in the cubic YF$_3$ and LaF$_3$ are less negative compared to those in ScF$_3$. This quantitative inconsistency between the mode-Grüneisen parameters [Fig. 6] and the *ab initio* MD calculations [Fig. 7] should stem from the anharmonicity parameters and temperature-Grüneisen parameters [117], which are not included in QHA [118].

V. CONCLUSIONS

The group-representation theory qualitatively predicted the emergence of ORDs in the $Pm\bar{3}m$ phases of ScF$_3$, YF$_3$, AlF$_3$, GaF$_3$, and InF$_3$, not in the $Pm\bar{3}m$ phase of LaF$_3$. We have found that the suppression of ORD in the $Pm\bar{3}m$ phases of ScF$_3$ and YF$_3$ stems from the scarce energy-stabilization terms because of their large band gaps and long bond lengths. We have also found that the delicate balance between the repulsive force term and the energy-stabilization term gives rise to the low frequency of the R_4^+ phonon, which is crucial for the NTE behavior. From this perspective, we have computationally predicted that the metastable cubic YF$_3$ and LaF$_3$ exhibit NTE behaviors. Combining all the discussions, we can obtain a simple conclusion that the following two conditions are essential to realizing the NTE behavior: (i) the preservation of high crystal symmetry, and (ii) large average atomic volumes in pristine materials. The first condition can be perceived from the mode-Grüneisen parameters and thermal expansion behaviors in the $Pm\bar{3}m$ and $R\bar{3}c$ phases in ScF$_3$ [Fig. 2]. The second condition can be understood from the thermal expansion behaviors in the $Pm\bar{3}m$ phases of ScF$_3$, YF$_3$, and LaF$_3$ [Fig. 7], indicating the larger NTE behavior as the cation size increases. The SOJT effect is a pivotal indicator for considering the preservation of high crystal symmetry. We believe that our study would provide an understanding of a material design principle for realizing NTE.
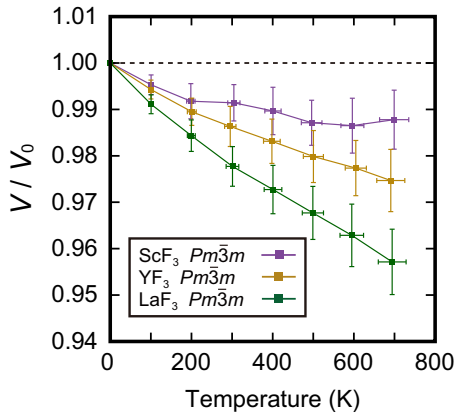
FIG. 7. Equilibrium volumes of the cubic YF$_3$ and LaF$_3$ derived from the *ab initio* MD calculations performed with the on-the-fly machine-learning force field. The error bars as the standard deviations for temperature and volumes are also indicated.

[1] K. Scheel, Versuche ueber die ausdehnung fester koerper, insbesondere von quarz in richtung derhauptachse, platin, palladium und quarzglas bei der temperatur der fluessigen luft, Verh. Dtsch. Phys. Ges. **9**, 3 (1907).

[2] K. Scheel, Ueber die ausdehnung des quarzglases, Verh. Dtsch. Phys. Ges. **9**, 719 (1907).

[3] C. Martinek and F. A. Hummel, Linear thermal expansion of three tungstates, J. Am. Ceram. Soc. **51**, 227 (1968).

[4] B. K. Greve, K. L. Martin, P. L. Lee, P. J. Chupas, K. W. Chapman, and A. P. Wilkinson, Pronounced negative thermal expansion from a simple structure: Cubic ScF_3, J. Am. Chem. Soc. **132**, 15496 (2010).

[5] M. Dapiaggi and A. N. Fitch, Negative (and very low) thermal expansion in ReO_3 from 5 to 300 K, J. Appl. Crystallogr. **42**, 253 (2009).

[6] T. Chatterji, P. F. Henry, R. Mittal, and S. L. Chaplot, Negative thermal expansion of ReO_3: Neutron diffraction experiments and dynamical lattice calculations, Phys. Rev. B **78**, 134105 (2008).

[7] T. A. Mary, J. S. O. Evans, T. Vogt, and A. W. Sleight, Negative thermal expansion from 0.3 to 1050 kelvin in ZrW_2O_8, Science **272**, 90 (1996).

[8] J. S. O. Evans, T. A. Mary, T. Vogt, M. A. Subramanian, and A. W. Sleight, Negative thermal expansion in ZrW_2O_8 and HfW_2O_8, Chem. Mater. **8**, 2809 (1996).

[9] Y. Yamamura, N. Nakajima, and T. Tsuji, Calorimetric and x-ray diffraction studies of α-to-β structural phase transitions in HfW_2O_8 and ZrW_2O_8, Phys. Rev. B **64**, 184109 (2001).

[10] N. Khosrovani, A. Sleight, and T. Vogt, Structure of $ZrV_2 O_7$ from -263 to 470 °C, J. Solid State Chem. **132**, 355 (1997).

[11] K. M. White, P. L. Lee, P. J. Chupas, K. W. Chapman, E. A. Payzant, A. C. Jupe, W. A. Bassett, C.-S. Zha, and A. P. Wilkinson, Synthesis, symmetry, and physical properties of cerium pyrophosphate, Chem. Mater. **20**, 3728 (2008).

[12] J. Evans, T. Mary, and A. Sleight, Negative thermal expansion in $Sc_2(WO_4)_3$, J. Solid State Chem. **137**, 148 (1998).

[13] P. Forster and A. Sleight, Negative thermal expansion in $Y_2W_3O_{12}$, Int. J. Inorg. Mater. **1**, 123 (1999).

[14] P. Forster, A. Yokochi, and A. Sleight, Enhanced negative thermal expansion in $Lu_2W_3O_{12}$, J. Solid State Chem. **140**, 157 (1998).

[15] B. A. Marinkovic, M. Ari, R. R. de Avillez, F. Rizzo, F. F. Ferreira, K. J. Miller, M. B. Johnson, and M. A. White, Correlation between A O_6 polyhedral distortion and negative thermal expansion in orthorhombic $Y_2Mo_3O_{12}$ and related materials, Chem. Mater. **21**, 2886 (2009).

[16] C. P. Romao, F. A. Perras, U. Werner-Zwanziger, J. A. Lussier, K. J. Miller, C. M. Calahoo, J. W. Zwanziger, M. Bieringer, B. A. Marinkovic, D. L. Bryce, and M. A. White, Zero thermal expansion in $ZrMgMo_3O_{12}$: NMR crystallography reveals origins of thermoelastic properties, Chem. Mater. **27**, 2633 (2015).

[17] H. Miyazaki, I. Ushiroda, D. Itomura, T. Hirashita, N. Adachi, and T. Ota, Thermal expansion of $NaZr_2(PO_4)_3$ family ceramics in a low-temperature range, Jpn. J. Appl. Phys. **47**, 7262 (2008).

[18] Y. Liu, M. S. Molokeev, Q. Liu, and Z. Xia, Crystal structures, phase transitions and thermal expansion properties of $NaZr_2(PO_4)_3$-$SrZr_4(PO_4)_6$ solid solutions, Inorg. Chem. Front. **5**, 619 (2018).

[19] T. Isobe, Y. Hayakawa, Y. Adachi, R. Uehara, S. Matsushita, and A. Nakajima, Negative thermal expansion in α-$Zr_2SP_2O_{12}$ based on phase transition- and framework-type mechanisms, NPG Asia Mater. **12**, 80 (2020).

[20] T. Amos and A. Sleight, Negative thermal expansion in orthorhombic $NbOPO_4$, J. Solid State Chem. **160**, 230 (2001).

[21] J. Wang, J. Deng, R. Yu, J. Chen, and X. Xing, Coprecipitation synthesis and negative thermal expansion of $NbVO_5$, Dalton Trans. **40**, 3394 (2011).

[22] X. Wang, Q. Huang, J. Deng, R. Yu, J. Chen, and X. Xing, Phase transformation and negative thermal expansion in $TaVO_5$, Inorg. Chem. **50**, 2685 (2011).

[23] N. Shi, A. Sanson, Q. Gao, Q. Sun, Y. Ren, Q. Huang, D. O. de Souza, X. Xing, and J. Chen, Strong negative thermal expansion in a low-cost and facile oxide of $Cu_2P_2O_7$, J. Am. Chem. Soc. **142**, 3088 (2020).

[24] N. Shi, A. Sanson, Q. Sun, L. Fan, A. Venier, D. Oliveira de Souza, X. Xing, and J. Chen, Strong negative thermal expansion of Cu_2PVO_7 in a wide temperature range, Chem. Mater. **33**, 1321 (2021).

[25] Y. Kadowaki, R. Kasugai, Y. Yokoyama, N. Katayama, Y. Okamoto, and K. Takenaka, Structural phase transition and giant negative thermal expansion in pyrophosphate $Zn_{2-x}Mg_xP_2O_7$, Appl. Phys. Lett. **119**, 201906 (2021).

[26] A. Sanson, F. Rocca, G. Dalba, P. Fornasini, R. Grisenti, M. Dapiaggi, and G. Artioli, Negative thermal expansion and local dynamics in Cu_2O and Ag_2O, Phys. Rev. B **73**, 214305 (2006).

[27] J. Li, A. Yokochi, T. G. Amos, and A. W. Sleight, Strong negative thermal expansion along the O−Cu−O linkage in $CuScO_2$, Chem. Mater. **14**, 2602 (2002).

[28] S. I. Ahmed, G. Dalba, P. Fornasini, M. Vaccari, F. Rocca, A. Sanson, J. Li, and A. W. Sleight, Negative thermal expansion in crystals with the delafossite structure: An extended x-ray absorption fine structure study of $CuScO_2$ and $CuLaO_2$, Phys. Rev. B **79**, 104302 (2009).

[29] K. W. Chapman and P. J. Chupas, Pressure enhancement of negative thermal expansion behavior and induced framework softening in zinc cyanide, J. Am. Chem. Soc. **129**, 10090 (2007).

[30] A. Phillips, A. Goodwin, G. Halder, P. Southon, and C. Kepert, Nanoporosity and exceptional negative thermal expansion in single-network cadmium cyanide, Angew. Chem. Int. Ed. **47**, 1396 (2008).

[31] Q. Gao, J. Wang, A. Sanson, Q. Sun, E. Liang, X. Xing, and J. Chen, Discovering large isotropic negative thermal expansion in framework compound $AgB(CN)_4$ via the concept of average atomic volume, J. Am. Chem. Soc. **142**, 6935 (2020).

[32] A. L. Goodwin, M. Calleja, M. J. Conterio, M. T. Dove, J. S. O. Evans, D. A. Keen, L. Peters, and M. G. Tucker, Colossal positive and negative thermal expansion in the framework material $Ag_3[Co(CN)_6]$, Science **319**, 794 (2008).

[33] G. Shirane and S. Hoshino, On the phase transition in lead titanate, J. Phys. Soc. Jpn. **6**, 265 (1951).

[34] M. Azuma, W.-t. Chen, H. Seki, M. Czapski, S. Olga, K. Oka, M. Mizumaki, T. Watanuki, N. Ishimatsu, N. Kawamura, S. Ishiwata, M. G. Tucker, Y. Shimakawa, and J. P. Attfield, Colossal negative thermal expansion in $BiNiO_3$ induced by intermetallic charge transfer, Nat. Commun. **2**, 347 (2011).

[35] H. Yamamoto, T. Imai, Y. Sakai, and M. Azuma, Colossal negative thermal expansion in electron-doped $PbVO_3$ perovskites, Angew. Chem. Int. Ed. **57**, 8170 (2018).

[36] H. Ishizaki, Y. Sakai, T. Nishikubo, Z. Pan, K. Oka, H. Yamamoto, and M. Azuma, Negative thermal expansion in lead-free la-substituted $Bi_{0.5}Na_{0.5}VO_3$, Chem. Mater. **32**, 4832 (2020).

[37] Z. Pan, T. Koike, T. Nishikubo, L. Hu, Q. Liu, Y. Sakai, S. Kawaguchi, and M. Azuma, Realization of negative thermal expansion in lead-free $Bi_{0.5}K_{0.5}VO_3$ by the suppression of tetragonality, Inorg. Chem. **61**, 3730 (2022).

[38] K. Takenaka and H. Takagi, Giant negative thermal expansion in Ge-doped anti-perovskite manganese nitrides, Appl. Phys. Lett. **87**, 261902 (2005).

[39] S. Iikubo, K. Kodama, K. Takenaka, H. Takagi, M. Takigawa, and S. Shamoto, Local lattice distortion in the giant negative thermal expansion material $Mn_3Cu_{1-x}Ge_xN$, Phys. Rev. Lett. **101**, 205901 (2008).

[40] K. Takenaka, Y. Okamoto, T. Shinoda, N. Katayama, and Y. Sakai, Colossal negative thermal expansion in reduced layered ruthenate, Nat. Commun. **8**, 14102 (2017).

[41] H. Mizoguchi, J. Bang, T. Inoshita, T. Kamiya, and H. Hosono, On the origin of the negative thermal expansion behavior of YCu, Inorg. Chem. **58**, 11819 (2019).

[42] H. Boysen, B. Dorner, F. Frey, and H. Grimm, Dynamic structure determination for two interacting modes at the M-point in α- and β-quartz by inelastic neutron scattering, J. Phys. C **13**, 6127 (1980).

[43] M. T. Dove, V. Heine, and K. D. Hammonds, Rigid unit modes in framework silicates, Mineral. Mag. **59**, 629639 (1995).

[44] A. K. A. Pryde, K. D. Hammonds, M. T. Dove, V. Heine, J. D. Gale, and M. C. Warren, Rigid unit modes and the negative thermal expansion in ZrW_2O_8, Phase Trans. **61**, 141 (1997).

[45] M. G. Tucker, M. P. Squires, M. T. Dove, and D. A. Keen, Dynamic structural disorder in cristobalite: neutron total scattering measurement and reverse Monte Carlo modelling, J. Phys.: Condens. Matter **13**, 403 (2001).

[46] M. T. Dove, Flexibility of network materials and the rigid unit mode model: a personal perspective, Philos. Trans. A **377**, 20180222 (2019).

[47] Q. Li, K. Lin, Z. Liu, L. Hu, Y. Cao, J. Chen, and X. Xing, Chemical diversity for tailoring negative thermal expansion, Chem. Rev. **122**, 8438 (2022).

[48] W. Miller, C. W. Smith, D. S. Mackenzie, and K. E. Evans, Negative thermal expansion: a review, J. Mater. Sci. **44**, 5441 (2009).

[49] K. Takenaka, Negative thermal expansion materials: technological key for control of thermal expansion, Sci. Technol. Adv. Mater. **13**, 013001 (2012).

[50] J. Chen, L. Hu, J. Deng, and X. Xing, Negative thermal expansion in functional materials: controllable thermal expansion by chemical modifications, Chem. Soc. Rev. **44**, 3522 (2015).

[51] M. T. Dove and H. Fang, Negative thermal expansion and associated anomalous physical properties: review of the lattice dynamics theoretical foundation, Rep. Prog. Phys. **79**, 066503 (2016).

[52] N. Shi, Y. Song, X. Xing, and J. Chen, Negative thermal expansion in framework structure materials, Coord. Chem. Rev. **449**, 214204 (2021).

[53] Y. Mochizuki, H. Koiso, K. Nagamatsu, S. Bae, T. Isobe, and A. Nakajima, Thermal properties of the element and binary oxides toward negative thermal expansion: A first-principles lattice-dynamics study, J. Phys. Chem. C **128**, 525 (2024).

[54] C. R. Morelock, J. C. Hancock, and A. P. Wilkinson, Thermal expansion and phase transitions of α-AlF_3, J. Solid State Chem. **219**, 143 (2014).

[55] M. Roosand and G. Meyer, Refinement of the crystal structure of gallium trifluoride, GaF_3, Z. Kristallogr. - New Cryst. Struct. **216**, 18 (2001).

[56] R. Hoppe and D. Kissel, Zur kenntnis von AlF_3 und InF_3 [1], J. Fluor. Chem. **24**, 327 (1984).

[57] A. K. Cheetham and N. Norman, The structures of yttrium and bismuth trifluorides by neutron diffraction. Acta Chem. Scand. A **28**, 55 (1974).

[58] P. Modak, A. Verma, S. Ghosh, and G. Das, Pressure-induced phase transition in tysonite LaF_3, J. Phys. Chem. Solids **70**, 922 (2009).

[59] See Supplemental Material at http://link.aps.org/supplemental/10.1103/PhysRevB.110.064104 for the details of the ground-state crystal structures for YF_3 and LaF_3, and equilibrium lattice volumes of the six ground-state BF_3 derived from the *ab initio* MD calculations; the calculated phonon bands and mode-Grüneisen parameters for the ground-state structures of six BF_3 without external pressure and those for the $R\bar{3}c$ phase of ScF_3 under 1.5 GPa; the calculated electronic band structures for the $Pm\bar{3}m$ and $R\bar{3}c$ phases of six BF_3; total energy variation as a function of the atomic displacement of rotational phonon mode transforming as irrep $R_4^+(a, a, a)$ in six cubic BF_3; and the lowest mode-Grüneisen parameters and the relevant phonon frequencies of the $R\bar{3}c$ phases for AlF_3, GaF_3, and InF_3, which includes Refs. [4,54,60,110,111].

[60] M. I. Aroyo, A. Kirov, C. Capillas, J. M. Perez-Mato, and H. Wondratschek, Bilbao Crystallographic Server. II. Representations of crystallographic point groups and space groups, Acta Crystallogr. A **62**, 115 (2006).

[61] C. W. Li, X. Tang, J. A. Muñoz, J. B. Keith, S. J. Tracy, D. L. Abernathy, and B. Fultz, Structural relationship between negative thermal expansion and quartic anharmonicity of cubic ScF_3, Phys. Rev. Lett. **107**, 195504 (2011).

[62] M. T. Dove, Z. Wei, A. E. Phillips, D. A. Keen, and K. Refson, Which phonons contribute most to negative thermal expansion in ScF_3? APL Mater. **11**, 041130 (2023).

[63] M. T. Dove, J. Du, Z. Wei, D. A. Keen, M. G. Tucker, and A. E. Phillips, Quantitative understanding of negative thermal expansion in scandium trifluoride from neutron total scattering measurements, Phys. Rev. B **102**, 094105 (2020).

[64] C. Yang, P. Tong, J. C. Lin, X. G. Guo, K. Zhang, M. Wang, Y. Wu, S. Lin, P. C. Huang, W. Xu, W. H. Song, and Y. P. Sun, Size effects on negative thermal expansion in cubic ScF_3, Appl. Phys. Lett. **109**, 023110 (2016).

[65] L. Hu, F. Qin, A. Sanson, L.-F. Huang, Z. Pan, Q. Li, Q. Sun, L. Wang, F. Guo, U. Aydemir, Y. Ren, C. Sun, J. Deng, G. Aquilanti, J. M. Rondinelli, J. Chen, and X. Xing, Localized symmetry breaking for tuning thermal expansion in ScF_3 nanoscale frameworks, J. Am. Chem. Soc. **140**, 4477 (2018).

[66] S. Yoshida, H. Akamatsu, and K. Hayashi, Electronic origin of non-zone-center phonon condensation: Octahedral rotation as a case study, Phys. Rev. Lett. **127**, 215701 (2021).

[67] E. Grüneisen, Theorie des festen zustandes einatomiger elemente, Ann. Phys. **344**, 257 (1912).

[68] M. Blackman, On the thermal expansion of solids, Proc. Phys. Soc. B **70**, 827 (1957).

[69] T. Barron, Grüneisen parameters for the equation of state of solids, Ann. Phys. **1**, 77 (1957).

[70] R. G. Pearson, The second-order Jahn-Teller effect, J. Mol. Struct. (THEOCHEM) **103**, 25 (1983).

[71] P. García-Fernández, J. A. Aramburu, M. Moreno, M. Zlatar, and M. Gruden-Pavlovi, A practical computational approach to study molecular instability using the pseudo-Jahn-Teller effect, J. Chem. Theor. Comput. **10**, 1824 (2014).

[72] I. B. Bersuker, Pseudo-Jahn-Teller effect-a two-state paradigm in formation, deformation, and transformation of molecular systems and solids, Chem. Rev. **113**, 1351 (2013).

[73] J. M. Rondinelli, A. S. Eidelson, and N. A. Spaldin, Non-d^0 Mn-driven ferroelectricity in antiferromagnetic $BaMnO_3$, Phys. Rev. B **79**, 205119 (2009).

[74] T. Nagai, Y. Mochizuki, S. Yoshida, and T. Kimura, Chemical aspect of displacive-type ferroaxial phase transition from perspective of second-order Jahn-Teller effect: NASICON systems as an example, J. Am. Chem. Soc. **145**, 8090 (2023).

[75] M. S. Dresselhaus, G. Dresselhaus, and A. Jorio, *Group Theory: Application to the Physics of Condensed Matter* (Springer, Berlin, 1995).

[76] P. E. Blöchl, Projector augmented-wave method, Phys. Rev. B **50**, 17953 (1994).

[77] J. P. Perdew, A. Ruzsinszky, G. I. Csonka, O. A. Vydrov, G. E. Scuseria, L. A. Constantin, X. Zhou, and K. Burke, Restoring the density-gradient expansion for exchange in solids and surfaces, Phys. Rev. Lett. **100**, 136406 (2008).

[78] J. Heyd, G. E. Scuseria, and M. Ernzerhof, Hybrid functionals based on a screened coulomb potential, J. Chem. Phys. **118**, 8207 (2003).

[79] J. Heyd, G. E. Scuseria, and M. Ernzerhof, Erratum: hybrid functionals based on a screened coulomb potential J. Chem. Phys. **124**, 219906(E) (2006).

[80] A. V. Krukau, O. A. Vydrov, A. F. Izmaylov, and G. E. Scuseria, Influence of the exchange screening parameter on the performance of screened hybrid functionals, J. Chem. Phys. **125**, 224106 (2006).

[81] G. Kresse and J. Furthmüller, Efficient iterative schemes for *ab initio* total-energy calculations using a plane-wave basis set, Phys. Rev. B **54**, 11169 (1996).

[82] G. Kresse and D. Joubert, From ultrasoft pseudopotentials to the projector augmented-wave method, Phys. Rev. B **59**, 1758 (1999).

[83] A. Jain, S. P. Ong, G. Hautier, W. Chen, W. D. Richards, S. Dacek, S. Cholia, D. Gunter, D. Skinner, G. Ceder, and K. A. Persson, Commentary: The materials project: A materials genome approach to accelerating materials innovation, APL Mater. **1**, 011002 (2013).

[84] R. Jinnouchi, J. Lahnsteiner, F. Karsai, G. Kresse, and M. Bokdam, Phase transitions of hybrid perovskites simulated by machine-learning force fields trained on the fly with Bayesian inference, Phys. Rev. Lett. **122**, 225701 (2019).

[85] R. Jinnouchi, F. Karsai, and G. Kresse, On-the-fly machine learning force field generation: Application to melting points, Phys. Rev. B **100**, 014105 (2019).

[86] R. Jinnouchi, F. Karsai, C. Verdi, R. Asahi, and G. Kresse, Descriptors representing two- and three-body atomic distributions and their effects on the accuracy of machine-learned inter-atomic potentials, J. Chem. Phys. **152**, 234102 (2020).

[87] W. G. Hoover, A. J. C. Ladd, and B. Moran, High-strain-rate plastic flow studied via nonequilibrium molecular dynamics, Phys. Rev. Lett. **48**, 1818 (1982).

[88] D. J. Evans, Computer experiment for nonlinear thermodynamics of Couette flow, J. Chem. Phys. **78**, 3297 (1983).

[89] M. Parrinello and A. Rahman, Crystal structure and pair potentials: A molecular-dynamics study, Phys. Rev. Lett. **45**, 1196 (1980).

[90] M. Parrinello and A. Rahman, Polymorphic transitions in single crystals: A new molecular dynamics method, J. Appl. Phys. **52**, 7182 (1981).

[91] A. Togo, L. Chaput, T. Tadano, and I. Tanaka, Implementation strategies in phonopy and phono3py, J. Phys.: Condens. Matter **35**, 353001 (2023).

[92] A. Togo, First-principles phonon calculations with phonopy and phono3py, J. Phys. Soc. Jpn. **92**, 012001 (2023).

[93] A. Togo and I. Tanaka, First principles phonon calculations in materials science, Scr. Mater. **108**, 1 (2015).

[94] A. Togo, L. Chaput, I. Tanaka, and G. Hug, First-principles phonon calculations of thermal expansion in Ti_3SiC_2, Ti_3AlC_2, and Ti_3GeC_2, Phys. Rev. B **81**, 174301 (2010).

[95] A. Togo, F. Oba, and I. Tanaka, Transition pathway of CO_2 crystals under high pressures, Phys. Rev. B **77**, 184101 (2008).

[96] A. Togo, F. Oba, and I. Tanaka, First-principles calculations of the ferroelastic transition between rutile-type and $CaCl_2$-type SiO_2 at high pressures. Phys. Rev. B **78**, 134106 (2008).

[97] A. Togo and I. Tanaka, Evolution of crystal structures in metallic elements, Phys. Rev. B **87**, 184104 (2013).

[98] H. Akamatsu, K. Fujita, T. Kuge, A. Sen Gupta, A. Togo, S. Lei, F. Xue, G. Stone, J. M. Rondinelli, L.-Q. Chen, I. Tanaka, V. Gopalan, and K. Tanaka, Inversion symmetry breaking by oxygen octahedral rotations in the ruddlesden-popper $NaRTiO_4$ family, Phys. Rev. Lett. **112**, 187602 (2014).

[99] R. Dronskowski and P. E. Bloechl, Crystal orbital hamilton populations (COHP): energy-resolved visualization of chemical bonding in solids based on density-functional calculations, J. Phys. Chem. **97**, 8617 (1993).

[100] V. L. Deringer, A. L. Tchougréeff, and R. Dronskowski, Crystal orbital hamilton population (COHP) analysis as projected from plane-wave basis sets, J. Phys. Chem. A **115**, 5461 (2011).

[101] S. Maintz, V. L. Deringer, A. L. Tchougréeff, and R. Dronskowski, LOBSTER: A tool to extract chemical bonding from plane-wave based DFT, J. Comput. Chem. **37**, 1030 (2016).

[102] S. P. Ong, W. D. Richards, A. Jain, G. Hautier, M. Kocher, S. Cholia, D. Gunter, V. L. Chevrier, K. A. Persson, and G. Ceder, Python materials genomics (pymatgen): A robust, open-source python library for materials analysis, Comput. Mater. Sci. **68**, 314 (2013).

[103] V. Wang, N. Xu, J.-C. Liu, G. Tang, and W.-T. Geng, VASP-KIT: A user-friendly interface facilitating high-throughput computing and analysis using VASP code, Comput. Phys. Commun. **267**, 108033 (2021).

[104] D. Orobengoa, C. Capillas, M. I. Aroyo, and J. M. Perez-Mato, *AMPLIMODES*: symmetry-mode analysis on the Bilbao Crystallographic Server, J. Appl. Crystallogr. **42**, 820 (2009).

[105] J. M. Perez-Mato, D. Orobengoa, and M. I. Aroyo, Mode crystallography of distorted structures, Acta Crystallogr. A **66**, 558 (2010).

[106] H. T. Stokes, D. M. Hatch, and B. J. Campbell, ISODISTORT, ISOTROPY Software Suite.

[107] B. J. Campbell, H. T. Stokes, D. E. Tanner, and D. M. Hatch, *ISODISPLACE*: a web-based tool for exploring structural distortions, J. Appl. Crystallogr. **39**, 607 (2006).

[108] M. Iraola, J. L. Mañes, B. Bradlyn, M. K. Horton, T. Neupert, M. G. Vergniory, and S. S. Tsirkin, IrRep: Symmetry eigenvalues and irreducible representations of *ab initio* band structures, Comput. Phys. Commun. **272**, 108226 (2022).

[109] K. S. Aleksandrov, V. N. Voronov, A. N. Vtyurin, S. V. Goryainov, N. G. Zamkova, V. I. Zinenko, and A. S. Krylov, Lattice dynamics and hydrostatic-pressure-induced phase transitions in ScF_3, J. Exp. Theor. Phys. **94**, 977 (2002).

[110] D. Jones and W. Shand, Crystal growth of flourides in the lanthanide series, J. Cryst. Growth **2**, 361 (1968).

[111] C. R. Morelock, Thermal expansion, compressibility, and local structure of fluorides and oxyfluorides with the rhenium trioxide structure, Ph.D. thesis, Georgia Institute of Technology, 2014, https://repository.gatech.edu/entities/publication/9e6e13e6-f52a-4f72-b3dc-78e8c622666d.

[112] C. R. Morelock, B. K. Greve, M. Cetinkol, K. W. Chapman, P. J. Chupas, and A. P. Wilkinson, Role of anion site disorder in the near zero thermal expansion of tantalum oxyfluoride, Chem. Mater. **25**, 1900 (2013).

[113] Y. Mochizuki, H.-J. Sung, A. Takahashi, Y. Kumagai, and F. Oba, Theoretical exploration of mixed-anion antiperovskite semiconductors M_3XN(M = Mg, Ca, Sr, Ba; X = P, As, Sb, Bi), Phys. Rev. Mater. **4**, 044601 (2020).

[114] V. Popescu and A. Zunger, Effective band structure of random alloys, Phys. Rev. Lett. **104**, 236403 (2010).

[115] V. Popescu and A. Zunger, Extracting e versus $\vec{k}$ effective band structure from supercell calculations on alloys and impurities, Phys. Rev. B **85**, 085201 (2012).

[116] S. U. Handunkanda, E. B. Curry, V. Voronov, A. H. Said, G. G. Guzmán-Verri, R. T. Brierley, P. B. Littlewood, and J. N. Hancock, Large isotropic negative thermal expansion above a structural quantum phase transition, Phys. Rev. B **92**, 134101 (2015).

[117] Y. Shen, C. N. Saunders, C. M. Bernal, D. L. Abernathy, M. E. Manley, and B. Fultz, Anharmonic origin of the giant thermal expansion of NaBr, Phys. Rev. Lett. **125**, 085504 (2020).

[118] Y. Oba, T. Tadano, R. Akashi, and S. Tsuneyuki, First-principles study of phonon anharmonicity and negative thermal expansion in ScF_3, Phys. Rev. Mater. **3**, 033601 (2019).

[119] K. Momma and F. Izumi, VESTA3 for three-dimensional visualization of crystal, volumetric and morphology data, J. Appl. Crystallogr. **44**, 1272 (2011).